Wetting and Inductivity in the Impedance Behavior of Large Lithium-Ion Cells

F. J. Günter,[z] **J. Keilhofer, V. Böhm, R. Daub, and G. Reinhart**

Institute for Machine Tools and Industrial Management, Technical University of Munich, 85748 Garching, Germany

The wetting of the porous electrodes and the separator is crucial in the production of lithium-ion cells. Electrochemical impedance spectroscopy is able to measure and characterize the wetting. This paper p resents an equivalent circuit for commercial high-capacity cells and shows a method to analyze the wetting of these cells. The equivalent circuit includes an external inductance, a transmission line model (TLM) for the description of the pore impedance and, additionally, a TLM for the impedance of substrate foil inductance and contact resistance. Based on symmetric and full laboratory cells, the superposition of the impedance is discussed. Furthermore, the method to adjust the impedance and analyze the wetting is demonstrated on hard case cells with a capacity of 22 Ah. It is shown that, in addition to inductance for cables and electrode-external contacts, high-capacity lithium-ion cells build up inductance due to the electrode area in combination with the substrate foil. This inductance, together with the contact resistance, result in a characteristic hook in the Nyquist plot. A TLM describes and explains this behavior quite well. Additionally, the impedance of the cell is adjustable so that it corresponds to a laboratory cell in blocking conditions. Thus, the wetting of the separator and the wetting of the electrode become separately evaluable and calculable.

Since commercialization, the demand for lithium-ion cells has increased rapidly.[1] To achieve higher specific energy and energy density, the trend is toward large-format lithium-ion cells, especially in automotive or aerospace applications.[2–5] For economic production of these high-capacity cells, the industry is challenged to reduce costs while increasing (or at least maintaining) product quality over a complex linked process chain.[6–9]

The filling of the lithium-ion cells with electrolyte liquid contributes significantly to the costs of the cell.[10] During this process, the electrolyte is dosed into the cells and wets the porous media of electrode coatings as well as the porous separator.[11] Since the electrolyte realizes the ionic conductivity in the cell, a long time is waited until all the active material particles are accessed by the liquid.[10] Only then, first charging and discharging cycles are started to form a stable and homogeneous solid electrolyte interphase (SEI).[12,13]

One possibility to measure the wetting is the visualization of the electrolyte liquid by neutron radiography.[14–17] As the probes radiate after the measurement, the access to neutron sources is limited and the measurement instrumentation is complex and expensive,[18] visualization using X-rays[19] or lock-in thermography[20] were proposed for small pouch cells. Since the mass attenuation coefficients of the materials for substrate foil and housing (Al and Cu) as well as for the cathode active material (Fe, Mn, Co, Ni, etc..) are high compared to the elements of the electrolyte liquid (C, H, O, etc..),[21] the method is not suitable for large-format cells. Furthermore, due to the necessity of a contrast medium in the electrolyte[19] inline application is not feasible. In the case of lock-in thermography, the high excitation signals as well as the varnishing of the housing[22] could be critical to the quality and cannot be used as a non-destructive test without further examination. Apart from that, Deng et al. introduced ultrasonic scanning as a promising non-destructive method to visualize the wetting.[23]

Another powerful tool to measure and describe characteristics of lithium-ion cells and their components is electrochemical impedance spectroscopy (EIS): Hattendorff et al. used EIS to describe the resistance of the separator soaked with electrolyte.[24] Using an equivalent circuit based on a transmission line model (TLM), Ogihara measured the pore resistance and showed the influence of the coating thickness.[25,26] Due to the sufficient accuracy of TLMs in the description of the physical framework, the determination of the in-plane tortuosity,[27] the through-plane tortuosity[28] and the binder

migration[29] in electrodes was possible. Aging effects could also be assigned to increasing electrode resistances.[30,31]

EIS was used early to describe the wetting behavior of lithium-ion cells. Wu et al. reported the change and convergence of the impedance spectrum for small cylindrical cells (≈0.5 Ah) after dosing electrolyte and attributed the observations to the wetting.[32] This relation between EIS and the wetting was verified via neutron radiography later.[33] Also, a relative difference in impedance during wetting with different electrolytes was shown.[34] and EIS was used to characterize the influence of the electrolyte quantity.[35,36]

However, for wetting, either the whole spectrum or just the intercept resistance (in the Nyquist plot) was analyzed without modeling the impedance of the cell. Methods to describe wetting in depth are lacking, as current visualization methods cannot distinguish whether the liquid is on the macroscopic surfaces or in the pores. A differentiation of the wetting of separator and electrode was also not possible, yet.

Therefore, this paper presents an equivalent circuit model for large-format full cells, as well as a method to analyze and calculate the wetting of high-capacity cells. The equivalent circuit is derived from a general model taking into account the boundary conditions of the wetting process, the upscaling from laboratory to commercial cells and the superposition of measurement signals in full cells without reference electrode. The model results in a method to analyze the wetting. This method is exercised on symmetric and full Swagelok cells. Based on the experimental data and calculations, the superposition of electrodes in the impedance spectrum is discussed. Subsequently, the cell format is scaled up. The procedure is demonstrated on plug-in hybrid electric vehicle (PHEV)1 cells[37] presenting the results of the experiments.

Theory

The general equivalent circuit model.—Figure 1 (top) shows the electrode-separator assembly of a PHEV1 cell welded to the terminals of the housing cover. The mass of metallic connectors and their inductances (in relation to the resistance) are higher in comparison to coin or Swagelok cells. These electric conductors like tabs or bars are described by the impedance

$$Z_{\mathrm{B}i} = R_{\mathrm{B}i} + L_{\mathrm{B}i} \ (j\omega)^{\alpha_{\mathrm{B}i}} \approx L_{\mathrm{B}i} \ (j\omega)^{\alpha_{\mathrm{B}i}} \qquad [1]$$

with the inductance $L_{\mathrm{B}i}$, the resistance $R_{\mathrm{B}i}$ and depending on the complex angular frequency $j\omega$ (as well as $i \in \{1, 2\}$). The contacting

[z]E-mail: florian.guenter@iwb.tum.de
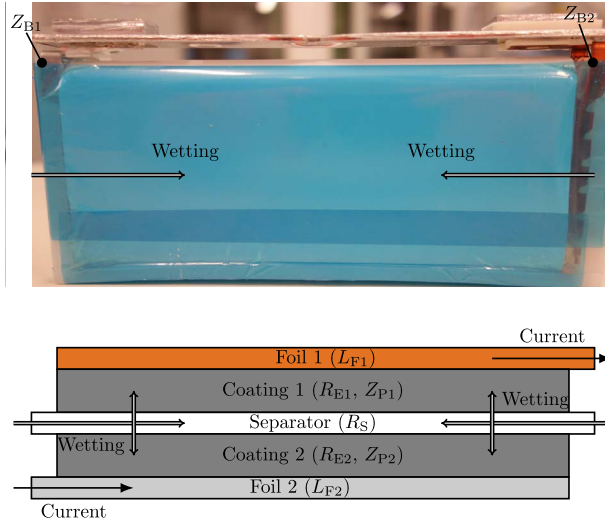
Figure 1. Picture of the electrode-separator-assembly of the PHEV1 cell (top) and schematic cross Section of the electrodes and the separator during wetting and electrical excitation (bottom).

bars are welded to the electrodes of the PHEV1 cell from opposite sides. Figure 1 (bottom) schematically shows a compartment of separator with resistance R_S and electrodes composed of substrate foils with inductance L_{Fi} and coatings with the pore impedance Z_{Pi} and R_{Ei}. In small cell geometries such as Swagelok cells, the current in the current collector solely occurs in cross-section. Thus, the distance the electrons travel is small (here 10 μm to 20 μm) and inductive phenomena do not occur. In contrast, in large format cells, current enters on one side, i.e. at the current collector. Hence, electrons also travel in in-plane direction throughout the whole current collector mm (here approximately 147.7 mm for the anode coating width) and inductive phenomena need to be considered.

Figure 2 depicts the general equivalent circuit model of a lithium-ion cell consisting of external conductors, two electrodes and a separator. Z_{Bi} describes the impedance of the electric conductors including cables, tab and/or bar as current collectors. Multiple incremental resistors r_S in-plane ($\parallel$) describe the separator soaked with electrolyte liquid $R_S = (\sum_{\parallel} (r_S)^{-1})^{-1}$. One electrode is composed of the impedance of the substrate foil with incremental inductance l_{Fi} and resistance r_{Fi}, of the coating with incremental resistance of the solid phase r_{Ei} as well as of the incremental elements r_{Pi} describing the resistance of the pores filled with electrolyte. The contact resistance at the interface between substrate foil and electrode coating is described by

$$z_{Ci} = \frac{r_{Ci}}{r_{Ci} \cdot q_{Ci} \ (j\omega)^{\alpha_{Ci}} + 1} \qquad [2]$$

with r_{Ci} for the contact resistance and q_{Ci} as capacitance for the double layer capacity at the interface between substrate foil and electrolyte liquid. The interface between the coating and the electrolyte is described by the charge transfer r_{Ti} elements and the capacitance of the double layer capacity q_{Ti}. For the overall resistance of the substrate foil, the contact resistance and the charge transfer resistance applies $R_{Fi} = \sum_{\parallel} r_{Fi}$, $R_{Ci} = (\sum_{\parallel} (r_{Ci})^{-1})^{-1}$ and $R_{Ti} = (\sum_{\parallel} (r_{Ti})^{-1})^{-1}$. The overall inductance of the substrate foil and the capacitance of the double layer capacity at the metal foil is calculated by $L_{Fi} = \sum_{\parallel} l_{Fi}$ and $Q_{Ci} = \sum_{\parallel} q_{Ci}$.[38] Here, the overall resistance of the solid differs in-plane or parallel to the separator with $R_{\parallel Ei} = \sum_{\parallel} r_{Ei}$ in comparison to through-plane or toward the separator ($\perp$) with $R_{\perp Ei} = \sum_{\perp} r_{Ei}$. This applies to the pure ionic pore resistance with $R_{\parallel Pi} = \sum_{\parallel} r_{Pi}$ and $R_{\perp Pi} = \sum_{\perp} r_{Pi}$ as well as the tortuosity and thickness of the direction and therefore the

number of elements in the sum differ. This difference is measurable with electrochemical impedance spectroscopy and was used by Suthar et al.[28] to determine and compare the tortuosity of electrodes in through-plane direction and in in-plane direction. This network of TLMs represents an electrode with connections in-plane as well as through-plane. The blue elements in Fig. 2 describe one slice of the electrode without considering in-plane linkages as it is used in literature for coin and Swagelok cells.[27,28,39]

The simplified equivalent circuit model.—Due to the high conductivity of the materials (aluminum or copper) and the large cross-sectional area of the external contacts R_{Bi} is neglected as already indicated by Eq. 1. Furthermore, the electrical conductivity in the materials for the substrate foil, as well aluminum or copper, is significant higher than in graphite based conductive agents or the active material of the electrodes ($R_{Fi} \ll R_{Ei}$). Therefore, R_{Fi} is negligible too. Here, the resistance in the solid phase in relation to the parallel resistance in the electrolyte liquid is considered negligible in in-plane direction $R_{\parallel Ei} \ll R_{\parallel Pi}$ as well as in through-plane direction $R_{\perp Ei} \ll R_{\perp Pi}$ according to Landesfeind et al.[39] As lithium intercalation/deintercalation is suppressed at 0% SOC as it is the case during wetting, blocking conditions are considered leading to $R_{Ti} \xrightarrow{wet.} \infty$.

As the electric resistances r_{Ei} are neglected, there are no potential gradients within the solid phase of the electrode coating. Due to homogeneity of the electrode, the network of impedances representing the porous electrode coating can be represented as identical TLMs in parallel. Hence, the network can be modeled as a single TLM ($Z_{Pi} = f(Q_{Ti}, R_{\perp Pi})$). As a result the model in Fig. 2 simplifies to an inductive element, an inductive TLM with contact impedances at the interface, a ionic TLM with ionic resistances and a constant phase elements at the interface and real resistance for the separator. All four contributions are connected in series. The impedance of the PHEV1 cell equates to

$$Z = Z_{B1} + Z_{C1} + Z_{P1} + R_S + Z_{P2} + Z_{C2} + Z_{B2} \qquad [3]$$

considering both electrodes, both external contacts and the separator. In this work, with the simplifications made, special case 3 is given for the TLM describing the inductivity and the contact impedance according to Ref. 38:

$$Z_{Ci} = \frac{\sqrt{Z_{Fi} \ Z_{Qi}}}{\tanh\left(\sqrt{\frac{Z_{Fi}}{Z_{Qi}}}\right)} \qquad [4]$$

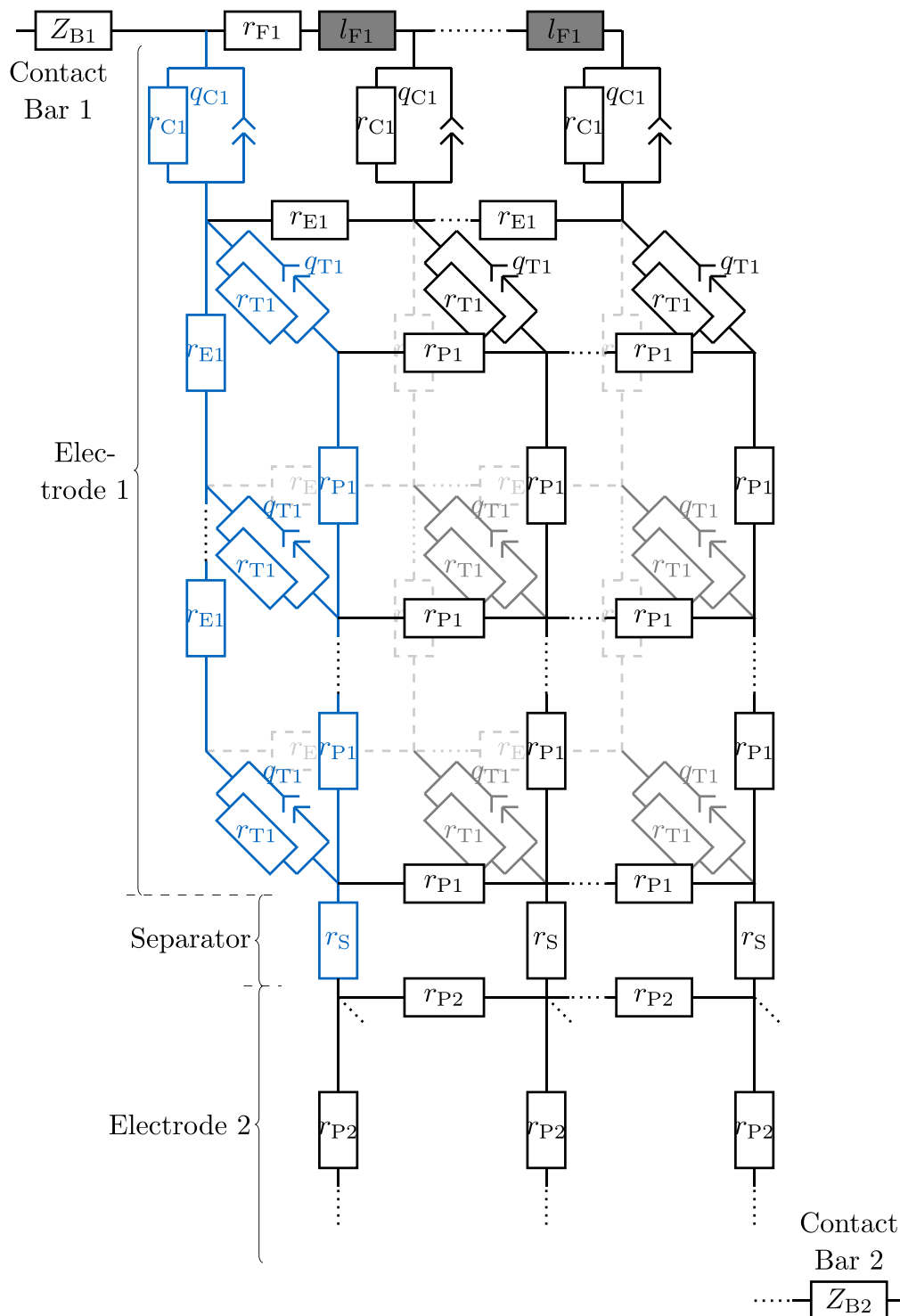with

$$Z_{Fi} = L_{Fi} \ (j\omega)^{\alpha_{Fi}} \qquad [5]$$

and

$$Z_{Qi} = \frac{R_{Ci}}{R_{Ci} \cdot Q_{Ci} \ (j\omega)^{\alpha_{Ci}} + 1} \qquad [6]$$

The impedance

$$Z_{Pi} = \frac{\sqrt{R_{Pi} \ (Q_{Ti} \ (j\omega)^{\alpha_{Ti}})^{-1}}}{\tanh\left(\sqrt{R_{Pi} \cdot Q_{Ti} \ (j\omega)^{\alpha_{Ti}}}\right)} \qquad [7]$$

is the solution for the transmission line model for the pore.[27]

For small capacity or laboratory cells like coin cells or Swagelok cells, the inductance L_{Bi} is often neglected. The resistance R_{Bi} is also either neglected or added to the separator resistance via the high frequency resistance (HFR). The same applies to inductances l_{Fi} and resistances r_{Fi} of the substrate foil of the electrodes as the distance of the foil is short (here $d = 10.95$ mm) and the conductivity of the foils

Figure 2. Equivalent circuit of a lithium-ion cell with current collector tabs. Z_{Bi} describe inductances originating from tabs, the contact bars and external contacts. The current collector is represented by incremental inductive elements l_{Fi} as well as incremental electric resistances r_{F1}. The contact impedance between current collector and electrode coating is represented by incremental RQ-elements z_{Qi}, i.e. resistances r_{C1} and constant phase elements q_{Ci} in parallel. The electrode coating is described by a network of resistances representing either the electric pathway in the solid r_{Ei} or the ionic pathway in the pores r_{Pi}. The transition from the electric pathway to the ionic pathway occurs via incremental resistances r_{Ti} and constant phase elements q_{Ti} in parallel representing the charge transfer reaction and the electrochemical double layer, respectively. The separator is represented by the incremental resistances r_S and connected to the ionic pathway.

is high.[24,27,31] Here, for the Swagelok cells, Eq. 3 is used with z_{Ci} instead of Z_{Ci}.

During wetting, the change in the impedance behavior is assumed to influence the resistance of the separator, which is according to Hattendorff et al.[24] dependent on the wetted area $R_S \propto A_{wet}^{-1}$.

Furthermore, the pore resistance R_{Pi} and the capacitance of the double layer capacity Q_{Ti} are assumed to change as the electrolyte soaks into the pores and opens up more area in the porous electrode to take part in the measurement. For simplicity, inductances, pure electrical as well as contact resistances, and the exponents describing the fractal

dimension (α_{xi}) are assumed constant over time. As the interfacial area between substrate foil and electrolyte liquid is very small compared to the interface of the porous coating to the electrolyte, the capacitance is accordingly small in relation $Q_{Ci} \ll Q_{Ti}$. Also because the wetting of the foil is irrelevant compared to the wetting of the pores, the change of the capacitance is negligible and Q_{Ci} is assumed constant. To analyze the wetting the impedance is calculated as follows:

$$Z_{\text{wet.}} = R_S + \underbrace{\underbrace{Z_{P1} + Z_{P2}}_{Z_P}}_{=f(t)}$$

$$= Z - \underbrace{(\underbrace{Z_{B1} + Z_{B2}}_{Z_B} + \underbrace{Z_{C1} + Z_{C2}}_{Z_C})}_{\approx \text{const.}} \qquad [8]$$

(For small capacity cells, z_{Ci} is used in Eq. 8 instead of Z_{Ci}). It is noted that for a detailed consideration at high frequencies and large electrode lengths the error neglecting the electrical resistances r_{Ei} in-plane increases. Then, due to different potentials, a representative pore would not be sufficient and a more complex modeling approach is necessary, which will be part of future work.

The superposition of electrodes.—For symmetric cells,[40] an impedance element of one electrode Z_{xi} (in Eq. 3) contributes half to the corresponding impedance element of the cell Z_x.[25,26] In full cells, three electrode setups allow the separated measurement of anode and cathode.[31,39] However, since there are no reference electrodes in commercial cells, only the working and counter electrodes are contacted during EIS-measurements for nondestructive testing. Then, the resulting signal is a superposition of all components. The clear assignment of an impedance element Z_{xi} to the anode or cathode is not possible without further knowledge of at least the impedance of one electrode. Here, the impedance of the full cell is described by combining the impedance elements in series to super-imposed elements:

$$Z_x = Z_{x1} + Z_{x2}$$
$$= f(R_{x1}/L_{x1}/Q_{x1}/\alpha_{x1}) + f(R_{x2}/L_{x2}/Q_{x2}/\alpha_{x2})$$
$$\approx f(R_x/L_x/Q_x/\alpha_x) = Z_{\overline{x}} \qquad [9]$$

with

$$R_x = R_{x1} + R_{x2}, \quad L_x = L_{x1} + L_{x2},$$
$$Q_x = \left(\frac{1}{Q_{x1}} + \frac{1}{Q_{x2}}\right)^{-1} \qquad [10]$$

and

$$\alpha_x = Q_x\left(\frac{\alpha_{x1}}{Q_{x1}} + \frac{\alpha_{x2}}{Q_{x2}}\right) \text{ or}$$
$$\alpha_x = \frac{L_{x1}\,\alpha_{x1} + L_{x2}\,\alpha_{x2}}{L_x} \qquad [11]$$

Thus, both electrodes are treated as one superimposed electrode calculated with parameters calculated from simplified series circuits. It is noted, that this assumption is correct for symmetric cells, but only approximately correct for full cells. Equations 9 to 11 presuppose the linearity of the functions in the Eqs. 1 to 7, which is generally not given for power functions and the hyperbolic tangent.

Equation 8 becomes

$$Z_{\overline{\text{wet.}}}(t) = R_S(t) + \frac{\sqrt{R_P(t)\,(Q_T(t)\,(j\omega)^{\alpha_T})^{-1}}}{\tanh\left(\sqrt{R_P(t) \cdot Q_T(t)\,(j\omega)^{\alpha_T}}\right)} \qquad [12]$$
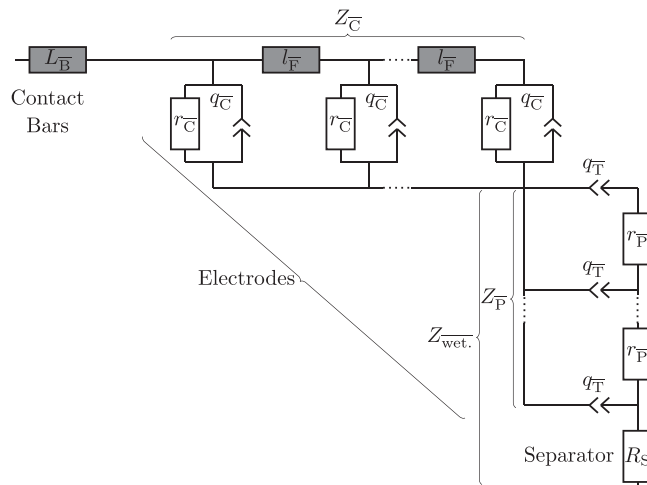
Figure 3. Simplified equivalent circuit model of a large-scale cell based on TLMs with a superposed electrode. The circuit includes inductances of external metallic contacts $L_{\overline{B}}$ and the substrate foils $l_{\overline{F}}$. The resistances are due to the contact between foil and solid phase $r_{\overline{C}}$, the solid phase of the porous electrode $r_{\overline{E}}$ itself as well as the pore resistance $r_{\overline{P}}$ and the resistance o the separator R_S. The double layer capacity between foil and electrolyte is described by the constant phase elements $q_{\overline{C}}$.

dependent on the time t during wetting. Figure 3 shows the simplified equivalent circuit model based on the two TLMs in series and with an superimposed electrode, which is used in this work.

Experimental

Sample preparation.—Both electrodes and the PHEV1 cells were produced at the *Center for Solar Energy and Hydrogen Research* (*ZSW*, Germany). The cathodes consisted of 95.5 w% LiNi$_{3/5}$Co$_{1/5}$Mn$_{1/5}$O$_2$ (NCM622; *BASF*, Germany) as active material, 2.25 w% carbon black, 0.75 w% SFG6L and 1.5 w% PVDF as binder. The anodes were composed of 94 w% graphite (SMGA5; *Hitachi*, Japan), 2 w% CMC and 3 w% SBR as binder and 1 w% C65. Further information about the electrode specifications are listed in Table I. The electrolyte *LP572* (*BASF*) used was a 1 M solution of LiPF$_6$ in a mixture of ethylene carbonate (EC) and ethyl methyl carbonate (EMC; weight ratio EC:EMC of 3:7) with 2 w% vinylene carbonate (VC).

For the Swagelok cells, one side of each electrode coil was delaminated. Distilled water was applied to the anode to solve the coating. Then, with a razor blade the coating was scapped from one side of the substrate foil. In case of the cathodes, N-Methyl-2-pyrrolidone (NMP) was used as a solvent. The electrode samples were punched out with a punch from *Nogami* (Japan) with a diameter of 10.95 mm. Glas fiber separators (*VWR*, Germany) with a thickness of 0.26 mm were punched to a diameter of 11 mm. Electrodes, separator and casing components of the Swagelok cells were dried in a *HCV* vacuum oven (*Hermann WALDNER GmbH & Co. KG*, Germany) in three loops under vacuum at 120 °C for 6 h in total right before cell assembly.

Eight symmetric Swagelok cells were built, four for the anode and four for the cathode cells. Per cell, two sealing rings were put into the screws and the plastic tube was mounted on the anode stamp. The first electrode and, then, two separators were put into the tube. 60 μl of electrolyte was dosed directly on top of the separator and the second electrode was mounted on the separator. The cathode die was put on the second electrode and a spring with 4.063 N mm^{-1} was mounted on the die. Using a micrometer screw, the spring was preloaded by 3 mm. Afterwards, the screw on the cathode side was tightened compressing the spring by 5.10 ± 0.14 mm in total.

Table I. Specifications of the electrodes used in the Swagelok cells as a symmetric and full-cell setup as well as in the PHEV1 cells. The values correspond to the coating of one electrode side. The electrodes of the PHEV1 cells were coated on both sides. The areal capacity was calculated using the theoretical values of 170 mAh g^{-1} for NCM622[41] and 355 mAh g^{-1} for the SMGA5.

	Anode	Cathode
Foil Thickness in μm	10 (Cu)	20 (Al)
Coating Thickness in μm	62 ± 0.92	49 ± 0.68
Porosity in %	37.47 ± 1.06	32.42 ± 0.88
Loading density in mg cm^{-2}	8.54 ± 0.08	14.53 ± 0.11
Areal capacity in mAh cm^{-2}	2.85 ± 0.03	2.36 ± 0.02
Footprint of Swagelok cells in cm^2	0.942 (=0.25π × 1.095^2)	0.942 (=0.25π × 1.095^2)
Footprint of PHEV1 cells in cm^2	6033.55 (=14.77 × 408.5)	5246.01 (=13.86 × 378.5)

Six full cells were built in the same way as the symmetric cells. Additionally, a gold wire reference electrode was used according to Ref.[42] A gold wire with cross-section diameter of 50 μm and a polyimide coating of 7 μm thickness (*Goodfellow GmbH*, Germany) was used. The coating was removed on one end, to ensure an electrical conductive contact between gold wire and the screw fixing the wire in the stamp of the reference electrode. Afterwards the gold wire was thread through an opening in the central T-cell body (and the plastic tube) during assembly. Hereby, the wire was placed between the two separators, to ensure it has no direct contact to one of the electrodes. Also an additional insulation ring was put between the reference stamp and the T-cell body.

The three PHEV1 hard case cells consisted of a flat wound cell assembly with an anode, a *Celgard 2325* (*Celgard*, United States of America) separator, a cathode and another *Celgard 2325*. The specifications of the electrodes are shown in Table I. The separator had a thickness of 25 μm and a porosity of 39%–41%.[43] Detailed information on the production processes are given in Ref.[36] For the filling process, the station was set up at the Technical University of Munich in a dry room with a dew point below −42 °C and a temperature of 19 °C.[6] The ambient pressure was 983 mbar. The evacuation pressure was set to 65 mbar. 90 ml electrolyte liquid was dosed into the cells via the first dosing pressure of 303 mbar and the second dosing pressure at the level of ambient pressure. After the second dosing step, the cells were vented.

To characterize the cells as well as the material system, they were tested after the wetting experiments. Results and procedures are listed in Table II as well as in the appendix (see Figs. A·1 to A·3).

Electrochemical impedance spectroscopy.—To investigate the impedance of the Swagelok cells a *VSP-3e* potentiostat (*BioLogic*, France) was used. The cells were connected on the anode and cathode side in a *MK-240* climate chamber (*Binder GmbH*, Germany) at 25 °C. Six frequencies per decade, within a frequency range from 1 MHz to 10 mHz, were chosen during the potentiostatic EIS-measurements. The amplitude of the input signal was set to 10 mV. Three measurements per frequency were performed to counter outliers. With this parameter setting, every 5.5 min a new impedance curve was generated. The impedance of the cells was measured for 24 h right after cell assembly including the dosing with electrolyte liquid. Only the last measurements were used per cell to exclude any changes.

After the dosing with electrolyte liquid into the PHEV1 cells, electrochemical impedance measurements were performed with an *Interface 5000E* potentiostat (*Gamry Instruments*, United States of America) for 210 min during the wetting process. The potentiostatic EIS was started at an initial frequency of 100 kHz and was changed to 1 Hz with 10 points per decade. Due to the low impedance of the large-format hard case cells used, the signal had to be adjusted to prevent the output currents from exceeding the limits of the potentiostat: An amplitude of 4 rms mV was applied as alternating current (AC) excitation signal to the cell. The constant potential offset that can be applied to the cell throughout the data acquisition

was set to zero versus the open circuit voltage (OCV) of the cell. The AC voltage was added to the direct current (DC) voltage.

Results and Discussion

The superposition of electrodes.—Figure 4 shows the the processing of the raw data Z of symmetric Swagelok cells up to the wetting impedance $Z_{wet.}$. The external inductance Z_B is in the symmetric anode cell clearly visible reaching positive imaginary values for high frequencies (Fig. 4 left). In the cathode cell, the contact resistance dominates, hiding the inductance. As the setup was the same except for the choice of electrodes for both cell types, the inductance $Z_{\overline{B}}$ was fitted using the anode cells, and subtracted from the impedance of both cell types. Figure 4 (middle) shows better recognizable the semicircle part of the contact resistance for the cathode, whereas the anode has almost no contact resistance. Fitting and subtracting the impedance of the respective contact resistances leaves only the impedance of the separator and porous electrode coating in Fig. 4 (right) over the whole frequency spectrum. The highest frequency begins for both cell types at the same point, because it is purely influenced by the separator, which was not changed in the setup. The parameter fitted for the cells are listed in Table A·1 in the appendix.

With Eqs. 10 and 11 the pore resistance of one electrode R_{Pi} is half the pore resistance of the cell R_P. The fractal dimension of an electrode and the symmetric cell is the same. The capacitance is twice that of the symmetric cell. In contrast, in full cells without reference electrode, the determination of electrode specific parameter is not feasible. It is possible to fit the superimposed signal to an equivalent circuit but the parameters may not always be physical reasonable.

The degree of similarity between the pore impedance of electrodes in the Nyquist plot is estimated from the ratios of the TLM parameters $\frac{\alpha_{T2}}{\alpha_{T1}}$, $\frac{R_{P2}}{R_{P1}}$, $\frac{Q_{T2}}{Q_{T1}}$ and $\frac{R_{P2}}{R_{P1}}\frac{Q_{T2}}{Q_{T1}}$. These ratios are equal to one for symmetric cells. Furthermore, $\frac{\alpha_{T2}}{\alpha_{T1}}$ is limited, as the fractional dimension of a constant phase element is at most equal to one for a two-dimensional surface (as for an ideal capacitor) or minimally equal to 0.5 for a three-dimensional surface (or a Warburg element).[44] In a cell, the ratio of the pore resistance is influenced by the thickness of the coating d_{Ei}, the tortuosity τ_{Ei} and the porosity Φ_{Ei} of the electrodes as $R_{Pi} \propto \frac{d_{Ei}\,\tau_{Ei}}{\Phi_{Ei}}$ applies.[27] The ratio of the capacitance is mainly determined by the active material surface of the different electrodes and, therefore, a function of the particle shape and the number of particles in the coatings.

The deviation of the approximation using one TLM for $Z_{\overline{P}} = f(R_P, Q_T, \alpha_T)$ in comparison to the sum of two electrode specific TLMs for $Z_{P1} + Z_{P2}$ with $Z_{Pi} = f(R_{Pi}, Q_{Ti}, \alpha_{Ti})$ was analyzed in the Nyquist plot: Fig. 5 shows the resulting root mean square error (RMSE) calculated using Eq. A·1 in the appendix. The farther a ratio deviates from one, the more different the electrodes are which leads to a greater error in the model as one superimposed electrode. Approximately, as long as $\frac{\alpha_{T2}}{\alpha_{T1}}$ does not deviate more than 20% from one and neither the resistance nor the capacitance of one electrode is

Table II. Results of the measured cells with C_N for the nominal capacity, E_m for the specific energy and E_V for the energy density at 0.2 C. The Swagelok cells were measured at 25 °C and the PHEV1 cells at 19 °C. * symbolizes values converted via the factor $\frac{\sigma_e(19\ °C)}{\sigma_e(25\ °C)} = 0.8924$ for an adjustment of the ionic conductivity from 19 °C to 25 °C. The measured weight of the Swagelok cells was 302.23 ± 1.25 g and 588.73 ± 0.17 g for the PHEV1 cells. The volume of the Swagelok cells was calculated to 37.32 ± 1.04 ml using Archimedes' principle. The volume of the PHEV1 cells is given by DIN91252[37] with 0.2774 L.

|	Swagelok sym. anode	Swagelok sym. cathode	Swagelok full cell	PHEV1 full cell
n	1	1	1	2
$A_{E,\ min}$ in cm^2	0.94	0.94	0.94	5246.01
$R_S(\infty)$ in Ω	5 ± 0.28	5.54 ± 0.53	5.22 ± 0.25	$(1.15 ± 0.1)\ 10^{-3}$
				$1.02 * 10^{-3}$
$z_{wet.}(\infty)$ in μm	492.37 ± 19.4	178.22 ± 6.64	—	—
τ_E	7.94 ± 0.31	3.66 ± 0.14	—	—
$R_P(\infty)$ in Ω	30.29 ± 1.05	12.67 ± 0.41	20.67 ± 0.4	$(2.73 ± 0.11)\ 10^{-3}$
				$2.44 * 10^{-3}$
$Q_T(\infty)$ in F s$^{\alpha-1}$	$(4.32 ± 0.07)\ 10^{-4}$	$(6.57 ± 0.18)\ 10^{-4}$	$(5.77 ± 0.03)\ 10^{-4}$	8.14 ± 0.22
C_N in Ah	—	—	$(1.98 ± 0.03)\ 10^{-3}$	22.17 ± 0.26
E_m in W h kg^{-1}	—	—	$(24.02 ± 0.45)\ 10^{-3}$	138.56 ± 1.67
E_V in W h L^{-1}	—	—	$(194.55 ± 3.65)\ 10^{-3}$	294.08 ± 3.61
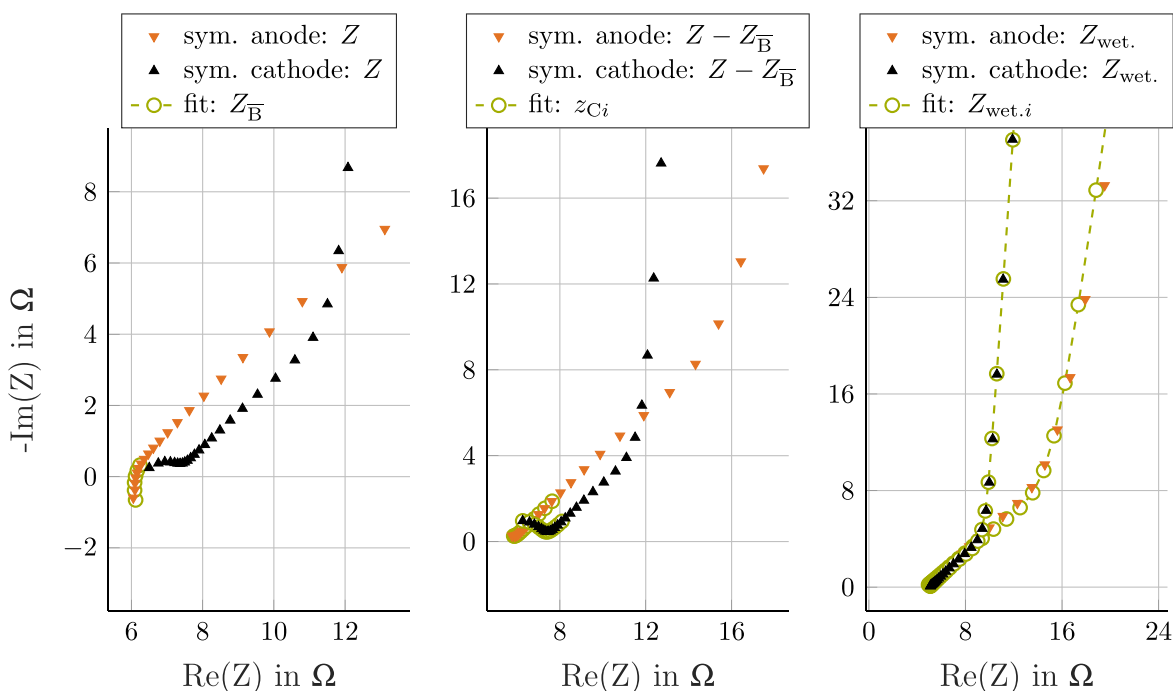
Figure 4. Nyquist plot of EIS measurements of a symmetric anode and cathode cell. 34 points between 456.64 kHz and 1.1 Hz of the measurements were used for the whole impedance analysis (excluding the two highest and the eleven lowest frequencies). Raw measurements and fit of the external inductance (to the electrodes) $Z_{\overline{B}}$ of cables and Swagelok casing via six points at high frequencies of 456.64 kHz to 64.35 kHz (left). Measurements of the symmetric cells adjusted for the inductance and fit of the superimposed contact resistances z_C of the electrodes via 14 points at high to mid frequencies of 456.64 kHz to 2.8 kHz (middle). Impedance adjusted for inductance and contact resistance to $Z_{wet.}$ with corresponding fit via 34 points from high to low frequencies of 456.64 kHz to 1.1 Hz (right).

at most twice as large as of the other electrode, the error remains below 10%. As shown by Fig. 5 (bottom left and right) the error stays low for $0.8 \leqslant \frac{\alpha_{T2}}{\alpha_{T1}} \leqslant 1.2$ even for high ratios of the resistance or the capacitance remains smaller than four times the product of resistance and capacitance as long as the product of resistance and capacitance remains smaller than four times the product of the other electrode. However, single frequencies have a higher error, since the Fig. only shows the mean value over the frequencies.

Based on the symmetric cells the ratio for the full cells was $\frac{\alpha_{T2}}{\alpha_{T1}} = 1.05$, $\frac{R_{P2}}{R_{P1}} = 0.42$, $\frac{Q_{T2}}{Q_{T1}} = 1.52$ and $\frac{R_{P2}\ Q_{T2}}{R_{P1}\ Q_{T1}} = 0.64$.

Figure 6 shows the wetting impedance $Z_{wet.}$ of the symmetric cells, the full cell and the modeled impedance using the fitted

parameter of the symmetric cells for two electrodes $Z_{P1} + Z_{P2}$ as well as for the superimposed electrode $Z_{\overline{P}}$. After the processing, all cells show in the Nyquist plot the typical blocking behavior as described in literature.[25–28,39] The full cell shows the same separator resistance as the symmetric cells due to the same setup regarding the separators. Furthermore, the pore resistance of the full cell spectrum lies between the lower pore resistance of the symmetric cathode cell and the higher pore resistance of the symmetric anode cell. The error of the two electrode model was 4.3 ± 2.1% and of the superimposed model 4.1 ± 2.1% compared to the measurement of the full cell. Thus, the deviation is within the modeling error. The fact that both models have the same error magnitude shows the validity of the
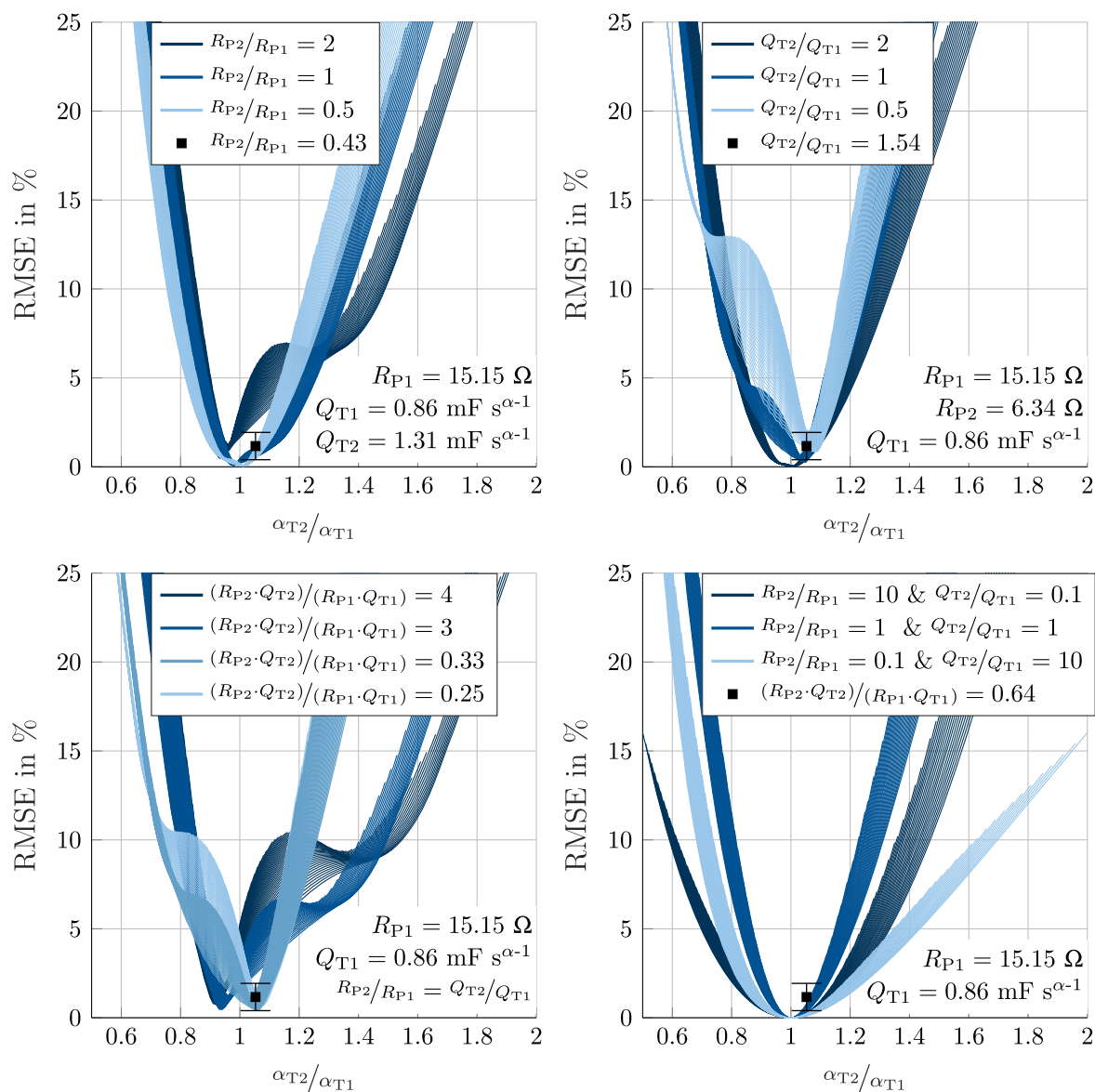
Figure 5. Root mean square error (RMSE; see Eq. A·1) between the pore impedance of the superimposed electrode $Z_{\bar{P}} = f(R_P, Q_T, \alpha_T)$ and the sum of the electrodes $Z_{P1} + Z_{P2}$ with $Z_{Pi} = f(R_{Pi}, Q_{Ti}, \alpha_{Ti})$ in the Nyquist plot calculated for 34 frequencies from 456.64 kHz to 1.1 Hz. The counter of the pore resistance ratio (top left), of the constant phase capacitance ratio (top right) and of the ratio of the products of resistance and capacitance (bottom left) was varied for all ratios of the fractal dimensions of two electrodes combined to one cell. The constant electrode parameters were based on the measured values of the symmetric cells (see Table A·1), with the indexes 1 for the anode and 2 for the cathode. The combination of the electrodes used in the symmetric setup are shown by the marker. The error bars show the standard deviation over the frequency. High ratios of resistance or capacitance for constant product ratios (bottom right).

simplification for the setup used. The fitted parameters of the cells with one TLM are shown in Table A·1 in the appendix. Furthermore, the deviation to the linear approximation of the parameters based on the symmetric cells as well as Eqs. 10 and 11 was 3.8% for the pore resistance, 10.7% for the double layer capacitance and 1.5% for the corresponding fractal dimension. Due to the still moderate error size, it is assumed that the analysis of an averaged electrode still allows physically meaningful conclusions for the electrode systems as well as the examined frequency range.

High capacity cells.—Figure 7 (left) shows the impedance spectrum of a representative PHEV1 (full) cell. The spectrum is in the Nyquist plot in the mΩ-range. Inductances, which pull the spectrum into the positive imaginary range, are clearly visible. After subtracting the external inductance with the fit $Z_{\bar{B}}$, a characteristic hook with spiral formation tendency is revealed in Fig. 7 (middle).

This shape is a result of the larger electrodes and internal inductances as described in the theory Section and by Fig. 3 (right). The hook is modelled as $Z_{\bar{C}}$ based on the Eq. 4 to Eq. 6 in the high to mid frequency range. After the adjustment for this transmission line equivalent circuit, Fig. 7 (right) displays a frequency response characteristic for laboratory cells in blocking conditions. As the resulting $Z_{\text{wet.}}$ describes only the impedance of separator and pores the wetting of the cell is evaluated for different points in time using the fit to $Z_{\overline{\text{wet.}}}$.

Figure 8 displays the evaluation of three PHEV1 cells during wetting. The separator resistance, the pore resistance (top left) and the double layer capacitance (top right) are shown over time. The resistances decrease and converge over time with increasing wetting as described in literature.[32,33] Based on the Eqs. from Hattendorff et al.[24] the resistance of the separator is expressed as a function of wetting
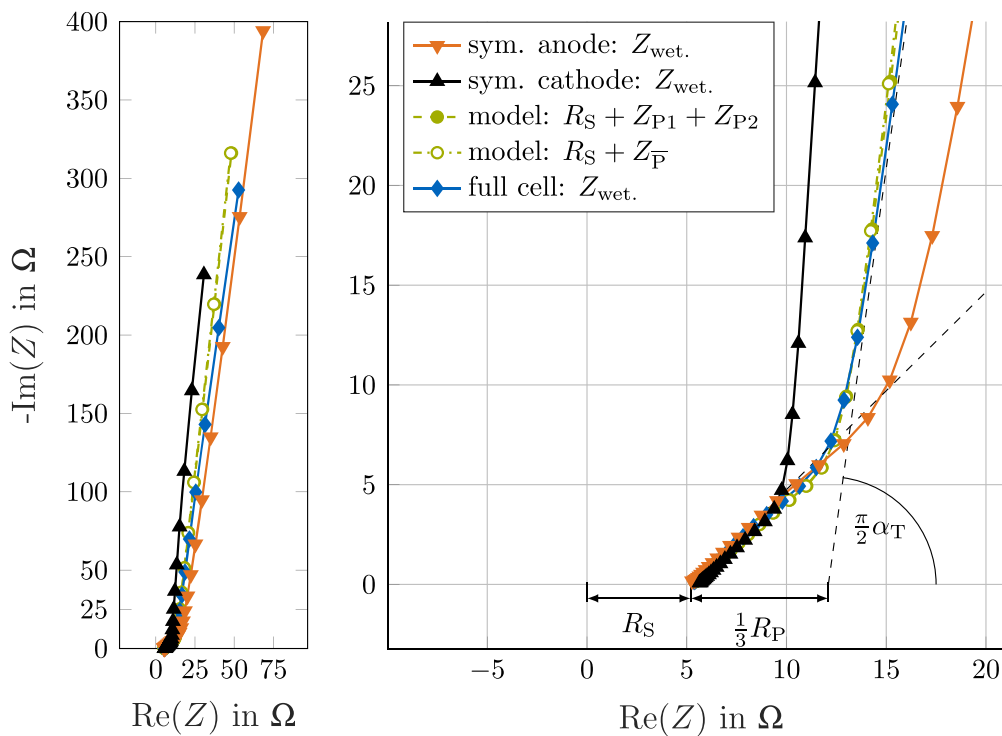
Figure 6. Nyquist plot of the symmetric cells and the Swagelok full cell 24 h after assembly for the 34 frequencies from 456.64 kHz to 1.1 Hz which were used to fit and model. Both models were based on the data of the symmetric cells.
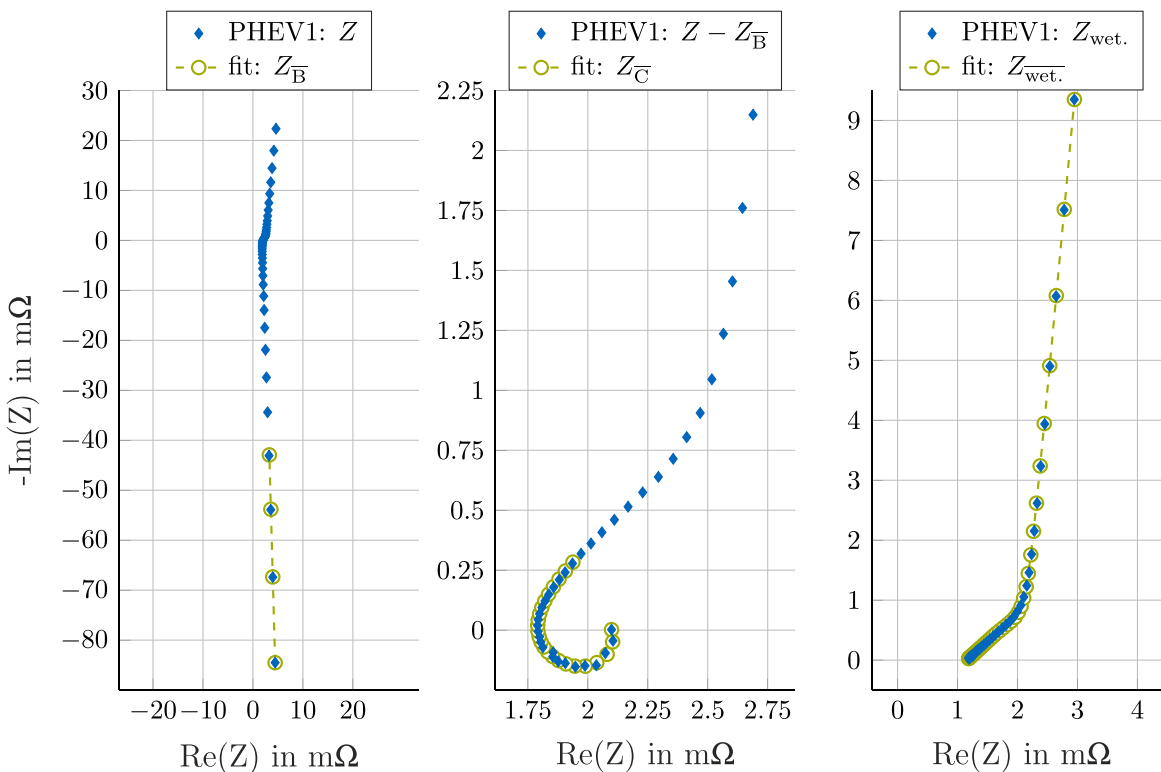
Figure 7. Nyquist plots of recorded and post-processed impedance data, as well as the according fits are shown. Part of the data (79.51 kHz to 39.9 kHz) were used to fit the external inductance $Z_{\overline{B}}$ representing cables and contact bars (left). Post-processed data with excluded external inductance were used to fit the inductive TLM in the upper frequency region between 79.51 kHz and 0.4 kHz describing the characteristic hook (middle). Further post-processed impedance data, corrected for the inductive TLM, and a fit according to Z_{wet} are shown (right).
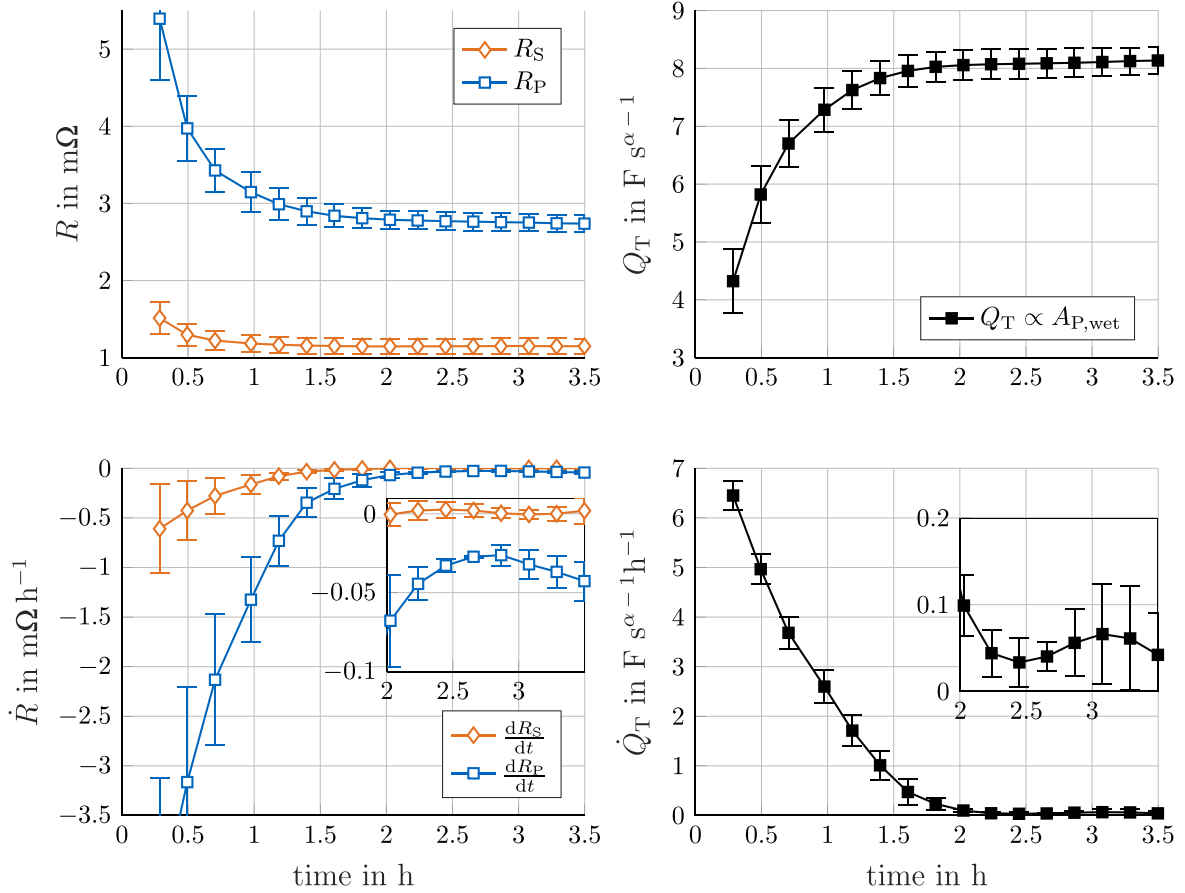
Figure 8. Separator resistance R_S and pore resistance R_P of the adjusted impedance $Z_{\overline{wet.}}$ of the PHEV1 cells over the wetting time after dosing electrolyte (top, left). Constant phase capacitance of the double layer capacity at the interface of porous electrode and electrolyte Q_T over the wetting time (top, right). Time derivative of the resistances (bottom, left) and the constant phase capacitance (bottom, right). Zero minutes describes the start of the dosing. The error bars depict the standard deviation of three cells at 19 °C.

$$R_S(t) = \frac{d_S \, \tau_S}{n \, \Phi_S \, \sigma_e} \, (A_{E,wet.}(t))^{-1}$$
$$= \frac{d_S \, \tau_S}{n \, \Phi_S \, \sigma_e} \, (x_{wet.}(t) \cdot y_{wet.}(t))^{-1} \qquad [13]$$

with the separator thickness d_S, the tortuosity τ, the porosity Φ, the conductivity of the electrolyte σ_e and $A_{E,wet.}(t \to \infty) = A_E$ as the minimum electrode footprint with a counter electrode. This footprint represents the footprint of the separator which takes part in the ionic charge transfer. n is the number of parallel circuits in the cell. For single layer cells (e.g. Swagelok cells), n is one and, for stacks or double-sided coatings $n \geqslant 2$. The separator resistance of the *Celgard 2325* with the electrolyt used in this work is given by literature with 2.8 Ωcm^{-2}.[24] With $A_E = 5246.01 \text{ cm}^2$ and $n = 2$ for the double-sided coating, $R_S(t \to \infty)$ is 1.07 mΩ which is similar to the measurement of the PHEV1 cell (converted to 25 °C) at the end of wetting (see Table II).

The footprint $A_{E,wet.}(t)$ wets with the time and is dependent on the wetting directions. For the wound cell assembly used in the PHEV1 cell, the wetting is just dependent on one macroscopic wetting axis $x(t)$ with $y(t) =$ constant.[17]

Regardless of the cell format, the wetting degree of the separator is given by

$$\phi_S(t) = \frac{x_{wet.}(t) \cdot y_{wet.}(t)}{A_E} = \frac{d_S \, \tau_S}{n \, \Phi_S \, \sigma_e \, A_E \, R_S(t)} \qquad [14]$$

and is therefore determinable without visualizing the wetting.

Figure 8 (bottom left) shows the time derivative of the resistances. The pore resistance changes significantly slower than the separator and is after 3.5 h still not at zero. Therefore, the separator is wetted first. Then, the electrode coating wets not only from the outer edges but also from separator surface. The Pore resistance of the full cell is given by

$$R_P(t) = \frac{1}{n \, A_E} \left(\frac{d_{E1} \, \tau_{E1} - z_{wet.1}(t)}{\sigma_g \, \Phi_{E1}} + \frac{z_{wet.1}(t)}{\sigma_e \, \Phi_{E1}} \right.$$
$$\left. + \frac{d_{E2} \, \tau_{E2} - z_{wet.2}(t)}{\sigma_g \, \Phi_{E2}} + \frac{z_{wet.2}(t)}{\sigma_e \, \Phi_{E2}} \right) \qquad [15]$$

with $z_{wet.i}(t)$ as the penetration distance of the electrolyte into the depth of the electrode pore (through-plane) and σ_g as the conductivity of the gas (mixture) in the pores, which is replaced by the electrolyte liquid during wetting. For complete wetting $z_{wet.i}(t \to \infty)$ is equal to $d_{Ei} \cdot \tau_{Ei}$ and for the pore resistance

$$R_P(t \to \infty) = \frac{1}{n \, A_E \, \sigma_e} \left(\frac{d_{E1} \, \tau_{E1}}{\Phi_{E1}} + \frac{d_{E2} \, \tau_{E2}}{\Phi_{E2}} \right) \qquad [16]$$

applies. The tortuosity was determined to 7.94 for the anode and 3.66 for the cathode using the method of Landesfeind et al.[27] on the symmetric Swagelok cells. With Eq. 16 and σ_{el} (25 °C) = 9.214 mS cm^{-1},[45] the pore resistance of the Swagelok full cell was calculated to 21.48 Ω which is a deviation of 3.9% to the fit (see Table II) 24 h after assembly. Thus, the deviation is within the modeling error. For the PHEV1 cells, 2.16 mΩ was calculated with σ_{el}(19 °C) = 8.223 mS cm^{-1}.[45]
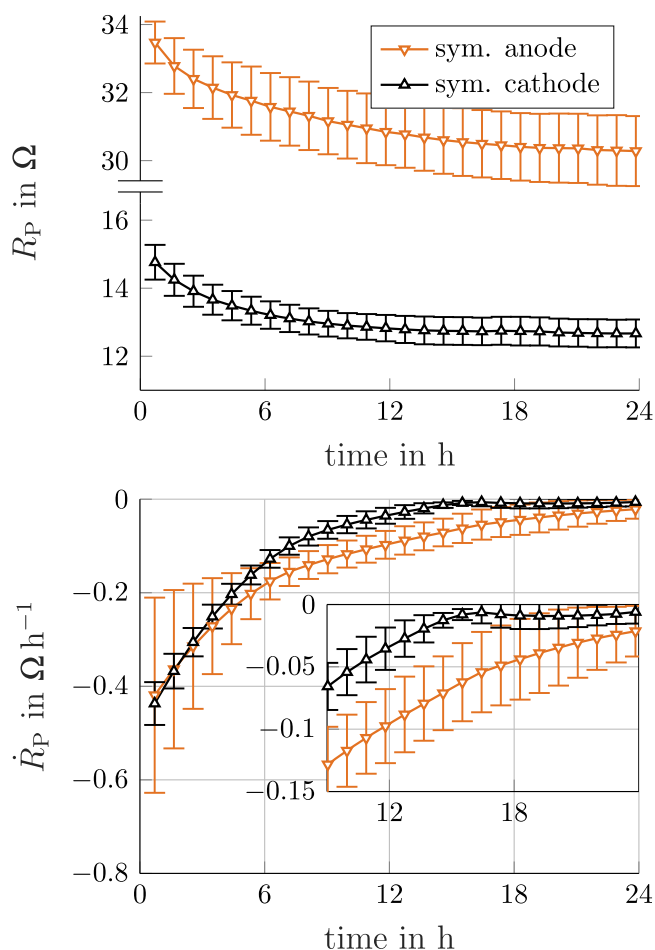
Figure 9. Pore resistance R_P of the adjusted impedance $Z_{\overline{\text{wet.}}}$ of the Swagelok cells over the wetting time after dosing electrolyte (left). Time derivative of the pore resistances (right). Zero minutes describes the end of the assembly. The error bars depict each the standard deviation of four cells at 25 °C.

The wetting degree of the pore is given by the two (over the footprint averaged) penetration depths for the electrodes $z_{\text{wet.i}}(t)$:

$$\phi_P(t) = \frac{z_{\text{wet.1}}(t) + z_{\text{wet.2}}(t)}{d_{E1}\,\tau_{E1} + d_{E2}\,\tau_{E2}}$$

$$\propto \frac{1}{R_P(t)\,n\,A_E\,\sigma_e}\left(\frac{d_{E1}\,\tau_{E1}}{\Phi_{E1}} + \frac{d_{E2}\,\tau_{E2}}{\Phi_{E2}}\right) \qquad [17]$$

Without reference electrode, it is not feasible to determine the respective $z_{\text{wet.i}}(t)$, but the measured pore resistance of the full cell suffices as an indicator. The pore resistance of the PHEV1 cell is after 3.5 h only at 2.73 mΩ. As the calculation based on the Swagelok cells for 19 °C indicated 2.16 mΩ, it is assumed that there are still pores in the electrodes which are not wetted:

Figure 9 shows the behavior of the pore resistance for 24 h after assembly of the symmetric Swagelok cells to differentiate between cathode and anode. As the electrolyte was dosed manually onto the electrodes, all macroscopic surfaces were wet during the assembly. Nevertheless, a change in the pore resistance was observed even 16 h after assembly for the cathode and even later for the anode, which has a longer wetting path $z_{\text{wet.}}(t \to \infty)$ as listed in Table II. It is noted that Swagelok and PHEV1 cell are not comparable in wetting speed or behavior. The PHEV1 cells were evacuated for the filling process.

Furthermore, the electrolyte in large format cells has to reach all surfaces before it can wet into the depth of all pores (in contrast to the Swagelok cells). However, the measurement shows that wetting mechanisms e.g. due to capillary forces or due to diffusion are still observable multiple hours after the electrolyte reached all macroscopic surfaces.

Figure 8 (right) displays additionally the influence on the double layer capacitance over time. In contrast to the resistance, the capacitance increases with upscaling of the cell format and with the wetting of electrolyte:

$$Q_T(t) = n\,\frac{\epsilon_0\,\epsilon}{d_H}\left(\frac{1}{A_{AM1}(t)} + \frac{1}{A_{AM2}(t)}\right)^{-1} \qquad [18]$$

Here, d_H is the thickness of the double layer, ϵ_0 is the absolute permittivity, ϵ the permitivity of the electrolyte and A_{AMi} the surface of active material. Without knowledge of the surface per active material particle, size and distribution or the number of particles it is difficult to determine a calculable relation. But the only time dependent variables are the wetted surfaces $A_{AMi}(t)$. These are dependent on the penetration depth and wetting of the respective electrode $z_{\text{wet.i}}(t)$. They increase and converge over time till the wetting is finished.

Conclusions

In this paper a novel circuit model was introduced, which considers the inductances of high capacity cells based on a transmission line model. Furthermore, a simplification via the superposition of the electrodes was used to fit the response signal in commercial cells without reference electrodes. A procedure to measure the wetting by adjusting for the inductances and contact resistances was shown on PHEV1 cells with a capacity of 22 Ah. The influence of the different electrodes as well as the upscaling of the cell format was discussed and shown on symmetric and full Swagelok cells in comparison to the PHEV1 cells.

The results show that a superimposed electrode model has only a small error for paired electrodes with a relation of the product of resistance and capacitance near to one. The substrate foils build up inductances in addition to external connectors which are observable as a characteristic hook in the Nyquist plot. After the adjustments, the Nyquist plot of a high capacity cell corresponds to a laboratory cell at lower impedance values and is easy to evaluate for the wetting. The wetting of the separator and the electrode is clearly distinguishable and shows the slower wetting of the electrodes, especially of the anodes. Without half-cell measurements it is not possible to distinguish between the electrodes. Only the complete wetting of both electrodes can be evaluated, since the superimposed electrodes are displayed in the full cell. Nevertheless, this work cannot only support the the identification and characterization of the wetting, but also be used to enhance prediction models with regards to early quality.[46,47]

Appendix

A·1. Impedance.—RMSE is defined as the mean error over the frequencies in the Nyquist plot

Table A·1. List of fitted impedance parameters of the measured cells at the end of wetting ($t \to \infty$). The Swagelok cells were measured at 25 °C and the PHEV1 cells at 19 °C.

Fitting parameter	Swagelok sym. anode	Swagelok sym. cathode	Swagelok full cell	PHEV1 full cell
L_B in H	$(5.14 \pm 1.28) \, 10^{-6}$	$(5.14 \pm 1.28) \, 10^{-6}$	$(5.14 \pm 1.28) \, 10^{-6}$	$(1.96 \pm 0.16) \, 10^{-7}$
α_B	0.8	0.8	0.8	0.979 ± 0.003
r_C in Ω	0.5 ± 0.24	1.95 ± 0.41	1.23 ± 0.48	—
q_C in F s$^{\alpha-1}$	$(2.56 \pm 2.16) \, 10^{-7}$	$(6.88 \pm 3.36) \, 10^{-7}$	$(3.35 \pm 2.77) \, 10^{-7}$	—
α_C	0.983 ± 0.035	0.908 ± 0.018	1	0.901 ± 0.011
R_C in Ω	—	—	—	$(3.58 \pm 0.28) \, 10^{-4}$
Q_C in F s$^{\alpha-1}$	—	—	—	$(3.49 \pm 0.19) \, 10^{-2}$
L_F in H	—	—	—	$(1.35 \pm 0.11) \, 10^{-6}$
α_F	—	—	—	0.604 ± 0.003
R_P in Ω	30.29 ± 1.05	12.67 ± 0.41	20.67 ± 0.4	$(2.73 \pm 0.11) \, 10^{-3}$
Q_T in F s$^{\alpha-1}$	$(4.32 \pm 0.07) \, 10^{-4}$	$(6.57 \pm 0.18) \, 10^{-4}$	$(5.77 \pm 0.03) \, 10^{-4}$	8.14 ± 0.22
α_T	0.91 ± 0.001	0.958 ± 0.002	0.915 ± 0.002	0.943 ± 0.001
R_S in Ω	5 ± 0.28	5.54 ± 0.53	5.22 ± 0.25	$(1.15 \pm 0.1) \, 10^{-3}$
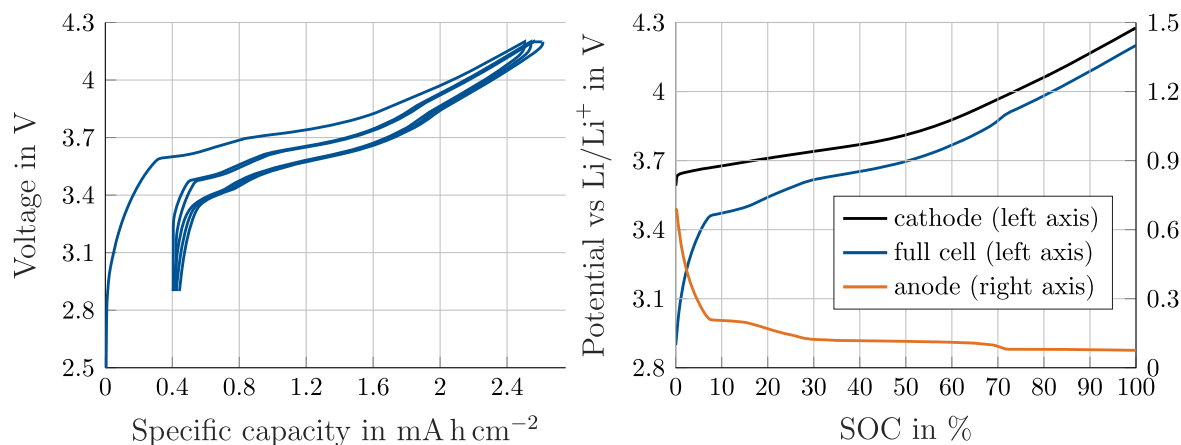
Figure A·1. Formation via three CC cycles of a representative full Swagelok cell at 0.2 C and 25 °C. The third cycle contains a CV phase during charging (left). Single electrode potentials and full cell voltage at charging with 0.1 C at 25 °C during the charge rate test (right).

$$\text{RMSE} = \frac{1}{k} \sum_k \frac{\sqrt{\text{Re}\,(Z_{\overline{P}} - Z_{P1} - Z_{P2})^2 + \text{Im}\,(Z_{\overline{P}} - Z_{P1} - Z_{P2})^2}}{\sqrt{\text{Re}\,(Z_{P1} + Z_{P2})^2 + \text{Im}\,(Z_{P1} + Z_{P2})^2}}$$

$$[\text{A·1}]$$

with k as the number of frequencies, Re(Z) as the real part and Im(Z) as the imaginary part of an impedance. Furthermore, the fitted impedance parameters of the measured cells at the end of wetting are listed in Table A·1.

A·2. Testing: Swagelok cells.—For the formation and cycling of the Swagelok full cells a *VSP-3e* potentiostat (*BioLogic*, France) was used. The cells were connected in a *MK-240* climate chamber (*Binder GmbH*, Germany) at 25 °C for all tests. First, a gold wire reference electrode[42] was lithiated with a constant current (CC) of 150 nA for 1 h after wetting. Then, the cells were twice charged and discharged in CC mode with 0.2 C corresponding to the theoretical capacity of the cells (see Table I for the electrode specifications). The upper cutoff voltage was set to 4.2 V and the lower cutoff voltage was set to 2.9 V. The third formation cycle had an additional constant voltage (CV) phase during charging with 0.02 C as lower

current limit. Figure A·1 (left) shows the resulting voltage over the specific capacity for a representative cell during formation.

Figure A·2 shows the charge rate test. It consisted of a CCCV discharge with always a current limitation of 0.02 C followed by a CC charge phase with the same cutoff voltages as during formation for multiple cycles. The C-rate was increased after three cycles from 0.1 C over 0.2 C to 0.5 C for the charge and discharge phase. Then the C-rate increased every five cycles from 1 C over 2 C, 3 C and 4 C to 5 C for charging. The discharge was set to 0.5 C. Between all the rates greater than 0.1 C a checkup cycle with 0.1 C for charge and discharge was implemented. The electrode and full potential is shown in Fig. A·1 (right) for the charge phase at 0.2 C.

A·3. Testing: PHEV1 cells.—The formation was carried out using a cell test system (*BasyTec*, Germany) and a temperature chamber at 19 °C. The cells were charged with 4.8 A constant current (CC). At the upper cutoff voltage of 4.2 V, the cells were charged with constant voltage (CV) till the current decreased to 1.2 A. The discharge was done in CC mode with 4.8 A and the lower cutoff voltage of 2.7 V. Afterwards, for complete formation, the charge and discharge cycle was repeated once.

The cells were sealed using blind rivets. The reversible capacities of the cells were determined by the discharge capacity
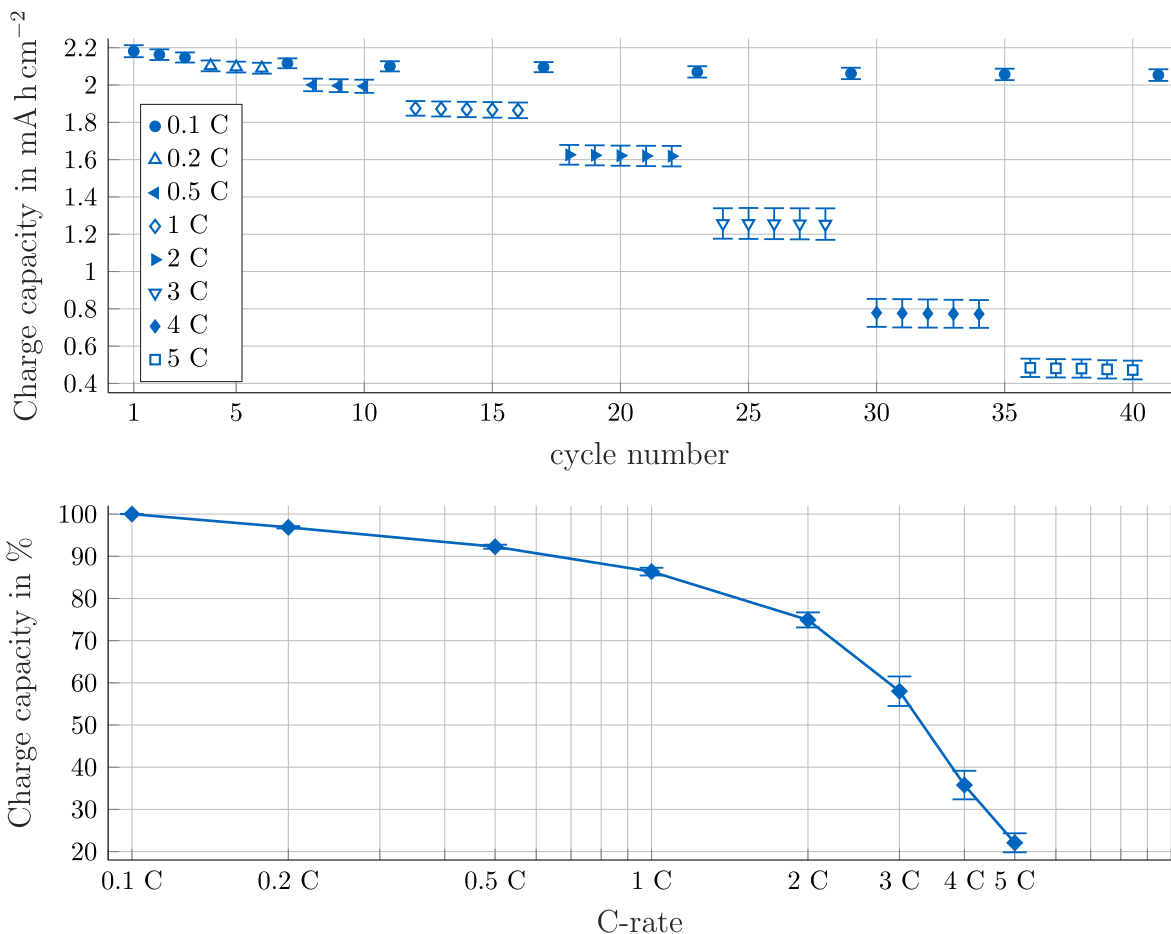
Figure A·2. Charge capacity during the charge rate test of the full Swagelok cells after formation. The error bars represent the standard deviation of six cells (top). Relative charge capacity as a function of the C-rate. For each cell the mean capacity of the first three cycles at 0.1 C was used as 100%. A marker depicts the mean value of the relative capacities calculated per cell and per C-rate. The error bars are the standard deviation of six cells and all cycles at the corresponding C-rate (bottom).
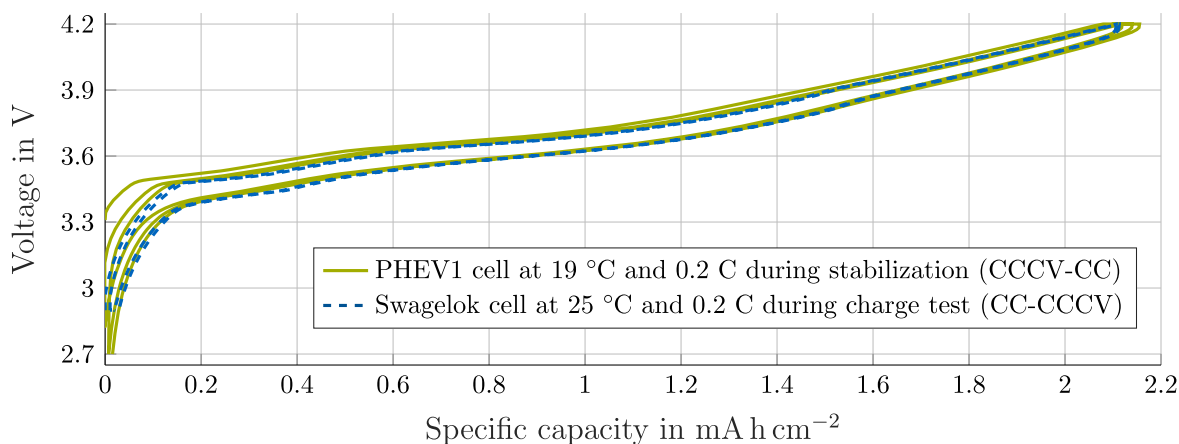
Figure A·3. Comparison of a Swagelok cell during charge rate testing at 0.2 C and 25 °C (CC-CCCV) to a PHEV1 cell during stabilization at 0.2 C and 19 °C (CCCV-CC).

of the second formation cycle. Back in the temperature chamber, three stabilization cycles were performed at 0.2 C (with the C-rate corresponding to the reversible capacity) and 19 °C in CCCV mode for charging with a current limitation corresponding to 0.05 C and in CC mode for discharging. The cutoff voltages were set to 4.2 V for charging and 2.7 V for discharging. The resulting cell properties can be found in Table II. Figure A·3 shows the voltage over the specific capacity during stabilization of the PHEV1 cell in comparison to a Swagelok cell during the charge test.

A.4.   List of symbols

Table A·2. List of symbols

latin symbols	description
A_{AM}	surface of the active material
A_E	footprint of the electrode coating
A_S	footprint of the separator
C_N	nominal capacity
d_E	thickness of the electrode coating
d_H	thickness of the double layer
d_S	thickness of the separator
E_m	specific energy
E_V	energy density
L_B	inductance of external electric conductors
l_F/L_F	(incremental) inductance of the electrode substrate foil
j	complex number
n	number of electrodes connected in parallel
q_C/Q_C	(incremental) capacitance of the double layer capacity at the substrate foil
q_T/Q_T	(incremental) capacitance of the double layer capacity at the electrode coating
r_C/R_C	(incremental) contact resistance between substrate foil and electrode coating
r_B/R_B	(incremental) resistance of external electric conductors
r_C/R_C	(incremental) contact resistance
r_E/R_E	(incremental) resistance of electrode coating (solid phase)
r_P/R_P	(incremental) pore resistance
r_S/R_S	(incremental) separator resistance
r_T/R_T	(incremental) charge transfer resistance
t	time
$x_{wet.}$	macroscopic wetting in x direction (in-plane)
$y_{wet.}$	macroscopic wetting in y direction (in-plane)
$z_{wet.}$	macroscopic wetting in z direction (through-plane)
Z_B	impedance of external electric conductors
z_C/Z_C	contact impedance of a small/high capacity cell
Z_P	pore impedance
$Z_{wet.}$	wetting impedance

Table A·3. List of symbols

greek symbols	description
α_B	fractal dimension of the conductor inductance
α_C	fractal dimension of the double layer capacity at the substrate foil
α_F	fractal dimension of the foil inductance
α_T	fractal dimension of the double layer capacity at the electrode coating
ϵ_0	absolute permittivity
ϵ	permittivity of the electrolyte
σ_g	ionic conductivity of the gas
σ_e	ionic conductivity of the electrolyte
ϕ_E	wetting degree of the electrode coating
ϕ_S	wetting degree of the separator
Φ_E	porosity of the electrode coating
Φ_S	porosity of the separator
ω	circular frequency

ORCID

F. J. Günter ⓘ https://orcid.org/0000-0002-5967-6801

References

1. A. Yoshino, "The birth of the lithium-ion battery." *Angewandte Chemie (International ed. in English)*, **51**, 5798 (2012).
2. J. Kurfer, M. Westermeier, C. Tammer, and G. Reinhart, "Production of large-area lithium-ion cells—preconditioning, cell stacking and quality assurance." *CIRP Annals*, **61**, 1 (2012).
3. D. Andre, S.-J. Kim, P. Lamp, S. F. Lux, F. Maglia, O. Paschos, and B. Stiaszny, "Future generations of cathode materials: An automotive industry perspective." *Journal of Materials Chemistry A*, **3**, 6709 (2015).
4. R. Schröder, M. Aydemir, and G. Seliger, "Comparatively assessing different shapes of lithium-ion battery cells." *Procedia Manufacturing*, **8**, 104 (2017).
5. F. J. Günter and N. Wassiliadis, "State of the art of lithium-ion pouch cells in automotive applications: cell teardown and characterization." *J. Electrochem. Soc.*, **169**, 030515 (2022).
6. G. Reinhart, T. Zeilinger, J. Kurfer, M. Westermeier, C. Thiemann, M. Glonegger, M. Wunderer, C. Tammer, M. Schweier, and M. Heinz, "Research and demonstration center for the production of large-area lithium-ion cells." *Future trends in production engineering*, ed. G. Schuh (Springer, Berlin, Heidelberg) 3 (2013).

7. G. Schuh (ed.), *Future trends in production engineering: Proceedings of the first conference of the German Academic Society for Production Engineering (WGP)* (Berlin, Springer) (2013), Berlin, Germany, 8th—9th june 2011.

8. T. Günther, N. Billot, J. Schuster, J. Schnell, F. B. Spingler, and H. A. Gasteiger, "The manufacturing of electrodes: Key process for the future success of lithium-ion batteries." *Advanced Materials Research*, **1140**, 304 (2016).

9. A. Kwade, W. Haselrieder, R. Leithoff, A. Modlinger, F. Dietrich, and K. Droeder, "Current status and challenges for automotive battery production technologies." *Nat. Energy*, **3**, 290 (2018).

10. D. L. Wood, J. Li, and C. Daniel, "Prospects for reducing the processing cost of lithium ion batteries." *Journal of Power Sources*, **275**, 234 (2015).

11. T. Knoche and G. Reinhart, "Electrolyte filling of large-scale lithium-ion batteries: Main influences and challenges for production technology." *Applied Mechanics and Materials*, **794**, 11 (2015).

12. E. Peled, "The electrochemical behavior of alkali and alkaline earth metals in nonaqueous battery systems—the solid electrolyte interphase model." *J. Electrochem. Soc.*, **126**, 2047 (1979).

13. S. J. An, J. Li, D. Mohanty, C. Daniel, B. J. Polzin, J. R. Croy, S. E. Trask, and D. L. Wood, "Correlation of electrolyte volume and electrochemical performance in lithium-ion pouch cells with graphite anodes and nmc532 cathodes." *J. Electrochem. Soc.*, **164**, A1195 (2017).

14. T. Knoche, V. Zinth, M. Schulz, J. Schnell, R. Gilles, and G. Reinhart, "In situ visualization of the electrolyte solvent filling process by neutron radiography." *Journal of Power Sources*, **331**, 267 (2016).

15. W. J. Weydanz, H. Reisenweber, A. Gottschalk, M. Schulz, T. Knoche, G. Reinhart, M. Masuch, J. Franke, and R. Gilles, "Visualization of electrolyte filling process and influence of vacuum during filling for hard case prismatic lithium ion cells by neutron imaging to optimize the production process." *Journal of Power Sources*, **380**, 126 (2018).

16. J. B. Habedank, F. J. Günter, N. Billot, R. Gilles, T. Neuwirth, G. Reinhart, and M. F. Zaeh, "Rapid electrolyte wetting of lithium-ion batteries containing laser structured electrodes: in situ visualization by neutron radiography." *The International Journal of Advanced Manufacturing Technology*, **273**, 966 (2019).

17. F. J. Günter, S. Rössler, M. Schulz, W. Braunwarth, R. Gilles, and G. Reinhart, "Influence of the cell format on the electrolyte filling process of lithium-ion cells." *Energy Technology*, **3**, 267 (2019).

18. M. Schulz and B. Schillinger, "Antares: Cold neutron radiography and tomography facility." *Journal of large-scale research facilities JLSRF*, **1**, A17 (2015).

19. A. Schilling, P. Gümbel, M. Möller, F. Kalkan, F. Dietrich, and K. Dröder, "X-ray based visualization of the electrolyte filling process of lithium ion batteries." *J. Electrochem. Soc.*, **166**, A5163 (2019).

20. A. Schilling, S. Wiemers-Meyer, V. Winkler, S. Nowak, B. Hoppe, H. H. Heimes, K. Dröder, and M. Winter, "Influence of separator material on infiltration rate and wetting behavior of lithium-ion batteries." *Energy Technology*, **4**, 1900078 (2019).

21. S. Seltzer, "Tables of x-ray mass attenuation coefficients and mass energy-absorption coefficients." Version 1.4 (2004), NIST standard reference database 126.

22. J. B. Robinson, E. Engebretsen, D. P. Finegan, J. Darr, G. Hinds, P. R. Shearing, and D. J. L. Brett, "Detection of internal defects in lithium-ion batteries using lock-in thermography." *ECS Electrochem. Lett.*, **4**, A106 (2015).

23. Z. Deng, Z. Huang, Y. Shen, Y. Huang, H. Ding, A. Luscombe, M. Johnson, J. E. Harlow, R. Gauthier, and J. R. Dahn, "Ultrasonic scanning to observe wetting and "unwetting" in li-ion pouch cells." *Joule*, **4**, 2017 (2020).

24. J. Hattendorff, J. Landesfeind, A. Ehrl, W. A. Wall, and H. A. Gasteiger, "Effective ionic resistance in battery separators." *ECS Trans.*, **69**, 135 (2015).

25. N. Ogihara, S. Kawauchi, C. Okuda, Y. Itou, Y. Takeuchi, and Y. Ukyo, "Theoretical and experimental analysis of porous electrodes for lithium-ion batteries by electrochemical impedance spectroscopy using a symmetric cell." *J. Electrochem. Soc.*, **159**, A1034 (2012).

26. N. Ogihara, Y. Itou, T. Sasaki, and Y. Takeuchi, "Impedance spectroscopy characterization of porous electrodes under different electrode thickness using a symmetric cell for high-performance lithium-ion batteries." *The Journal of Physical Chemistry C*, **119**, 4612 (2015).

27. J. Landesfeind, J. Hattendorff, A. Ehrl, W. A. Wall, and H. A. Gasteiger, *J. Electrochem. Soc.*, **163**, A1373 (2016).

28. B. Suthar, J. Landesfeind, A. Eldiven, and H. A. Gasteiger, "Method to determine the in-plane tortuosity of porous electrodes." *J. Electrochem. Soc.*, **165**, A2008 (2018).

29. R. Morasch, J. Landesfeind, B. Suthar, and H. A. Gasteiger, "Detection of binder gradients using impedance spectroscopy and their influence on the tortuosity of li-ion battery graphite electrodes." *J. Electrochem. Soc.*, **165**, A3459 (2018).

30. D. W. Abarbanel, K. J. Nelson, and J. R. Dahn, "Exploring impedance growth in high voltage nmc/graphite li-ion cells using a transmission line model." *J. Electrochem. Soc.*, **163**, A522 (2016).

31. D. Pritzl, J. Landesfeind, S. Solchenbach, and H. A. Gasteiger, "An analysis protocol for three-electrode li-ion battery impedance spectra: Part ii. analysis of a graphite anode cycled vs. lnmo." *J. Electrochem. Soc.*, **165**, A2145 (2018).

32. M.-S. Wu, T.-L. Liao, Y.-Y. Wang, and C.-C. Wan, "Assessment of the wettability of porous electrodes for lithium-ion batteries." *Journal of Applied Electrochemistry*, **34**, 797 (2004).

33. F. J. Günter, J. B. Habedank, D. Schreiner, T. Neuwirth, R. Gilles, and G. Reinhart, "Introduction to electrochemical impedance spectroscopy as a measurement method for the wetting degree of lithium-ion cells." *J. Electrochem. Soc.*, **165**, A3249 (2018).

34. R.-S. Kühnel, S. Obeidi, M. Lübke, A. Lex-Balducci, and A. Balducci, "Evaluation of the wetting time of porous electrodes in electrolytic solutions containing ionic liquid." *Journal of Applied Electrochemistry*, **43**, 697 (2013).

35. S. J. An, J. Li, C. Daniel, D. Mohanty, S. Nagpure, and D. L. Wood, "The state of understanding of the lithium-ion-battery graphite solid electrolyte interphase (sei) and its relationship to formation cycling." *Carbon*, **105**, 52 (2016).

36. F. J. Günter, C. Burgstaller, F. Konwitschny, and G. Reinhart, "Influence of the electrolyte quantity on lithium-ion cells." *J. Electrochem. Soc.*, **166**, A1709 (2019).

37. DIN 91252:2016-11, Electrically propelled road vehicles - Battery systems - Design specifications for Lithium-Ion battery cells.

38. H. Göhr, *Electrochemical Applications*, p. 2 (1997), ZAHNER-Elektrik GmbH & Co. KG.

39. J. Landesfeind, D. Pritzl, and H. A. Gasteiger, "An analysis protocol for three-electrode li-ion battery impedance spectra: Part i. analysis of a high-voltage positive electrode." *J. Electrochem. Soc.*, **164**, A1773 (2017).

40. C. Chen, J. Liu, and K. Amine, "Symmetric cell approach and impedance spectroscopy of high power lithium-ion batteries." *Journal of Power Sources*, **96**, 321–8 (2001).

41. M. Armand et al., "Lithium-ion batteries—current state of the art and anticipated developments." *Journal of Power Sources*, **479**, 228708 (2020).

42. S. Solchenbach, D. Pritzl, E. J. Y. Kong, J. Landesfeind, and H. A. Gasteiger, "A gold micro-reference electrode for impedance and potential measurements in lithium ion batteries." *J. Electrochem. Soc.*, **163**, A2265 (2016).

43. D. P. Finegan, S. J. Cooper, B. Tjaden, O. O. Taiwo, J. Gelb, G. Hinds, D. J. Brett, and P. R. Shearing, "Characterising the structural properties of polymer separators for lithium-ion batteries in 3d using phase contrast x-ray microscopy." *Journal of Power Sources*, **333**, 184 (2016).

44. P. Kurzweil and O. K. Dietlmeier (ed.), *Elektrochemische Speicher* (Wiesbaden, Springer Fachmedien Wiesbaden) (2015).

45. F. J. Günter, J. Keilhofer, C. Rauch, S. Rössler, M. Schulz, W. Braunwarth, R. Gilles, R. Daub, and G. Reinhart, "Influence of pressure and temperature on the electrolyte filling of lithium-ion cells: Experiment, model and method." *Journal of Power Sources*, **517**, 230668 (2022).

46. S. Stock, A. Ceruti, F. J. Günter, and G. Reinhart, "Introducing inline process and product analysis for the lean cell finalization in lithium-ion battery production." *Procedia CIRP*, **104**, 1052 (2021).

47. S. Stock, S. Pohlmann, F. J. Günter, L. Hille, J. Hagemeister, and G. Reinhart, "Early quality classification and prediction of battery cycle life in production using machine learning." *Journal of Energy Storage*, **50**, 104144 (2022).